Magnetic properties of $Cd_{1-x}Mn_xTe$/C nanocrystals

2011 Nanotechnology 22 075703

(http://iopscience.iop.org/0957-4484/22/7/075703)

Nanotechnology **22** (2011) 075703 (7pp) doi:10.1088/0957-4484/22/7/075703

Magnetic properties of $Cd_{1-x}Mn_xTe$/C nanocrystals

Sayan Bhattacharyya[1,4], **D Zitoun**[2,3] **and A Gedanken**[2,4]

[1] Department of Chemical Sciences, Indian Institute of Science Education and Research, Kolkata, Mohanpur-741252, Nadia, WB, India
[2] Department of Chemistry and Kanbar Laboratory for Nanomaterials at the Bar-Ilan University Center for Advanced Materials and Nanotechnology, Bar-Ilan University, Ramat-Gan 52900, Israel
[3] ICGM-AIME, Université Montpellier II, CC15, Place Bataillon 34095 Montpellier, France

E-mail: sayanb@iiserkol.ac.in and gedanken@mail.biu.ac.il

Received 18 June 2010, in final form 14 November 2010
Published 14 January 2011
Online at stacks.iop.org/Nano/22/075703

Abstract
Mn doped CdTe nanocrystals coated by carbon ($Cd_{1-x}Mn_xTe$/C) were synthesized by a one-step, kinetically controlled solid state reaction under autogenic pressure at elevated temperatures. Electron microscopic analysis confirmed that the 40–52 nm $Cd_{1-x}Mn_xTe$ core was encapsulated by a 6–9 nm carbon shell. The efficient doping by Mn^{2+} in the zinc blende $Cd_{1-x}Mn_xTe$ lattice, up to an atomic ratio of Mn/Cd of 0.031, was confirmed from electron paramagnetic resonance (EPR) experiments. In the case of higher doping, it is likely that manganese is partially expelled to the nanocrystal surface. All the doped samples exhibit ferromagnetism at room temperature. The lowest doped sample has the highest magnetic moment ($1.91 \pm 0.02\ \mu_B$/Mn). The more concentrated samples exhibit weaker ferromagnetic interactions, probably due to an incomplete coupling between carriers in the host CdTe semiconductor and dopant spins.

1. Introduction

In recent years there has been a growing interest in magnetoelectronic devices based on the control of charge as well as spin of the electrons. In this context diluted magnetic semiconductor (DMS) materials have been intensively studied in an effort to integrate them with electronic devices [1]. DMS is traditionally defined as a well characterized diamagnetic semiconductor doped with few to several atomic per cent of a transition metal with unpaired d-electrons. In the Mn^{2+} doped II–VI semiconductor nanocrystals, sp–d exchange interaction exists between the electron/hole band states of the semiconductors and the $Mn^{2+}3d^5$ electron states, whereby Mn^{2+} acts as a paramagnetic center ($S = 5/2$).

One of the most researched properties in DMS systems is room temperature ferromagnetism. In spite of the fact that II–VI DMS materials have lower ferromagnetic transition temperatures as compared to the III–V counterparts [2], the former are the most studied from both fundamental and application points of view, since localized spins and holes can be introduced and controlled independently in these systems. The ferromagnetic ground state can arise due to several kinds of dopant–dopant interactions that can couple the dopant spins in a DMS system. The most desirable and promising mechanism is carrier-mediated exchange interaction, where the dopant spins are coupled by itinerant electrons or holes in the host semiconductor, as observed in p-type Mn-based DMS [3]. However, the optical, electronic, or magnetic properties in these materials largely depend on the synthesis techniques employed, concentration of the dopants, particle size, and functional groups present on the surface of the nanocrystals.

Among the II–VI semiconductors, doping of manganese atoms into the cadmium telluride (CdTe) lattice has been studied [4–7], where CdTe is an intrinsic semiconductor with a room temperature band gap of 1.44 eV. Even though most of the DMS studied recently present a large bandgap (like ZnO or GaN), the ability to dope a semiconductor with optical properties in the visible region of the spectrum is very appealing. Doping CdTe with magnetic impurities has been rarely attempted and/or has been almost unsuccessful according to the very few articles found in the literature [8]. Indeed, Mn has a tendency to be expelled to the semiconductor

[4] Authors to whom any correspondence should be addressed.

nanocrystal surface due to the self-purification process [4, 9]. In order to obtain high quality DMS nanocrystals, it is important that manganese is actually embedded within the semiconductor host lattice for use in spin electronics and quantum information technology.

The strong demand for newer materials and functionalities, has led to recent progress in device fabrication technology based on the use of these nanocrystals as elemental building blocks for the next generation of spintronic nano-devices and biomedical engineering applications including contrast enhancing agents for magnetic resonance imaging. The majority of the applications require the functionalization of the nanocrystal surface, and CdTe nanocrystals have been capped/coated with a spectrum of functional groups such as thiol moieties [10, 11], bovine serum albumin [12], and L-cysteine facilitated positively charged quantum dots [13]. Post-treatment of the immobilized nanocrystals is sometimes disadvantageous, because fluorescent quantum yield typically decreases due to the surface coating. However, it has been observed that coating ZnSe nanocrystals with carbon enhanced the blue luminescence [14], and also carbon coating on DMS/semiconductor nanocrystals actually led to the stability of the luminescent properties, whereby continuous exposure to high-energy electron-beam only led to $<10\%$ decrease in luminescence efficiency after which it remained constant even after prolonged exposure to ambient conditions [15, 16]. Moreover, carbon in its various forms such as diamond, graphite, disordered, or amorphous has been used as a successful coating material to increase biocompatibility for biological/biomedicinal applications [17]. The carbon coating is particularly useful for the biologically toxic II–VI semiconductors and DMS nanocrystals to render them biocompatible.

Unlike the lengthy procedures of capping the nanostructures, a range of carbon coated DMS nanocrystals were synthesized by a one-step solid state reaction under autogenic pressure and elevated temperatures. This method has been successful for other doped semiconductors such as Mn doped ZnSe [15], Mn doped CdSe [17], Co doped ZnO [18], Mn doped ZnTe [19], and Mn doped TiO_2 [20]. The main advantage of the method is to use a gas state reaction between the chemicals with a self-limiting growth due to the formation of the carbon shell. On the one hand, compared to most of the solution phase methods, this reaction pathway allows the formation of highly crystalline compounds due to the high temperature used. On the other hand, compared to the physical methods, this route yields grams of nanomaterials that allow a full characterization of the dopant contribution to the magnetic property. Moreover, this method has the advantage of easy scale-up of the products based on the size of the reactor and the amount of starting materials, leading to large-scale production. In this paper, we have synthesized the Mn^{2+} doped CdTe nanocrystals coated with carbon and studied their magnetic properties. Manganese was found to be efficiently doped into the CdTe host lattice and all the doped nanocrystals demonstrate room temperature ferromagnetism.

2. Experimental details

2.1. Materials

The chemicals used do present the best purity available from commercial sources. Cadmium acetate dihydrate ($C_4H_6O_4Cd{\cdot}2H_2O$, Aldrich, 98%), manganese (II) acetate tetrahydrate ($C_4H_6O_4Mn{\cdot}4H_2O$, Fluka, >99%), and tellurium powder (30 mesh, Aldrich, 99.997%) were used as received. All the reactants were handled inside a N_2 filled glove box.

2.2. Synthesis

The synthesis method of Mn doped CdTe nanostructures coated with carbon involves mixing $C_4H_6O_4Cd{\cdot}2H_2O$, $C_4H_6O_4Mn{\cdot}4H_2O$ (according to the Mn:Cd atomic ratios of 0–0.04) along with excess Te. The mixture was filled inside a quartz tube fitted within a 5 ml stainless steel reactor, sealed, and heated inside a tubular furnace at 10 °C min^{-1}, maintained at 1000 °C for 6 h. The reactor was cooled (∼5 h) to ambient temperature, and the collected powder was sonicated in ethanol for 30 min. The dark liquid was decanted to remove the free carbonaceous species, and dried under vacuum. The yield of the gray colored $Cd_{1-x}Mn_xTe$/C products was ∼80% by weight.

2.3. Characterization

The obtained products were structurally characterized using inductively coupled plasma atomic emission spectroscopy (ICP-AES; Spectroflame Module E), transmission electron microscopy (TEM JEOL, 2010), elemental line scanning (WDX, JSM, 7000F) coupled to a high resolution scanning electron microscope (HRSEM, JSM, 7000F), and powder x-ray diffraction (Cu Kα = 1.5418 Å radiation, Bruker AXS D8). The EPR experiments were performed at X band ∼9.5 GHz on a Bruker ESP300 spectrometer with microwave powers between 0.02 and 200 mW. Magnetic properties were measured using a superconducting quantum interference design (SQUID) magnetometer MPMS XL7, in the temperature range of 2–300 K and fields varying between 0–5 T. The temperature-dependent susceptibility was measured using a DC procedure. The sample was cooled to 2 K under a zero magnetic field. A low magnetic field (5 mT) was applied and data were collected from 2 to 300 K (zero-field-cooled, ZFC). Field-cooled (FC) measurements were performed from 2 to 300 K with an applied field during the cooling. High temperature magnetic measurements were performed on a vibrating sample magnetometer (VSM) from Maglab Oxford Instrument operating at T = 300–900 K under a field of $\mu_0 H = 2$ T.

3. Results and discussion

The synthesis has been performed in a disposable cell to guarantee the lack of any contamination. The synthesis yields a gray powder (80% yield) that was analyzed by quantitative elemental analysis, x-ray diffraction, transmission electron microscopy, elemental analysis using scanning

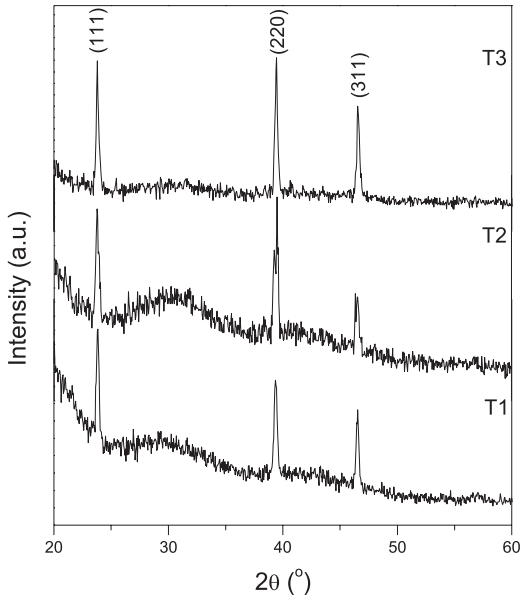

Figure 1. XRD patterns taken from the synthesized $Cd_{1-x}Mn_xTe$/C products.

electron microscopy, electron paramagnetic resonance, and magnetometry. The inductively coupled plasma (ICP) experiments revealed the bulk composition of the solid products according to the Mn:Cd atomic ratios of 0.0023(2), 0.0241(2), and 0.0313(1), and are designated as T1, T2, and T3, respectively, in subsequent discussions in the paper. To avoid contamination from the stainless steel reactor during the synthesis, the reactions were carried out inside a quartz tube fitted within the reactor. ICP analysis did not detect any iron or nickel in any of the powders. Even if any metallic impurities are present, the percentage is below the detection limit of ICP elemental analysis, so that the ICP measurements could not detect 0.01% Fe which might be present in the ratio of 0.0001 Fe atoms per Cd. The carbon weight percentages as determined from C, H, N analysis are 2.7, 3.3, and 3.5 for T1, T2, and T3, respectively. The x-ray diffraction (XRD) patterns of the $Cd_{1-x}Mn_xTe$/C products are shown in figure 1. The XRD peaks match well the pattern of zinc blende CdTe (JCPDS file No. 75-2086). All the indexed diffraction peaks are sharp and intense, resembling the high crystallinity of the nanocrystals. Assuming the nanocrystals are spherical, the average crystallite sizes calculated from the Scherrer formula after subtracting the instrumental broadening are 48 nm, 39 nm, and 43 nm for T1, T2, and T3, respectively. A broad hump is observed in the range $2\theta = 25°$–$35°$, which can be attributed to the surface crystalline features due to the carbon coating on the surface of the nanocrystals. XRD sharp peaks of carbon are not observed due to the amorphous or semi-crystalline nature of the encapsulating shell. According to Vegard's law, the lattice parameter of the $Cd_{1-x}Mn_xTe$ lattice should vary as 6.4807, 6.4776, and 6.4765 Å for T1, T2, and T3, respectively, if all the incorporated manganese remains within the CdTe lattice. Incidently, a shift of the (111) peak towards lower angle by $\Delta 2\theta = 0.01°$ from T1 to T2 to T3 was observed, justifying the former statement.

TEM images of the doped samples in figure 2 show the core–shell morphology where the shell is composed of carbon with lighter contrast around the DMS core. The thickness of the carbon shell is nearly the same, 6–9 nm in all the samples. The dimensions of the $Cd_{1-x}Mn_xTe$ core are 52 ± 5 nm, 40 ± 7 nm, and 46 ± 6 nm for T1, T2, and T3, respectively. As evident from the images, there is a wide distribution in the nanocrystal size. In order to investigate the core–shell morphology, the elemental line scanning of the nanocrystals in T3 (placed on a Si wafer) is shown in figure 3. The C-line shows intense humps at the nanocrystal edges, which are due to an excess of carbon at the shell. Both Cd and Te lines show a huge rise in concentration within the nanocrystal region, the intensities of both the lines are nearly equal, which indicates approximately the 1:1 atomic ratio of Cd:Te. The intensity of the Mn signal also rises in the nanocrystal core region, but is weaker as compared to Cd and Te, owing to 3.1 at.% of Mn in T3. The core–shell morphology can be explained by the synthesis route explored. The nanocrystals are formed by a one-step, template-free, kinetically controlled process. At high temperature and pressure inside the closed reactor, the Cd- and Mn-acetates decompose into their gaseous state, along with gaseous Te. The decomposition follows similar steps as reported previously [17]. Tellurium evaporates above 990 °C and reacts with $(Cd_{1-x}Mn_x)$–O to form $Cd_{1-x}Mn_xTe$ via the reaction: $2Cd_{1-x}Mn_xO + 2Te \rightarrow 2Cd_{1-x}Mn_xTe + O_2$. All the products of the dissociation reaction are formed in the gas phase followed by solidification into the core–shell nanocrystals. The solidification rate of $Cd_{1-x}Mn_xTe$ is faster than carbon, and hence $Cd_{1-x}Mn_xTe$ crystallizes initially to form the core, followed by carbon, giving rise to the core–shell structure. A little stoichiometric excess of Te was added, since a lesser amount of Te, and at temperatures <1000 °C, retained small percentages of $Cd_{1-x}Mn_xO$ and Mn-oxide impurity phases. The gas phase reaction permits a perfect mixing of the reactants for the synthesis of a homogeneous distribution of manganese in the CdTe matrix. Once the concentration and the homogeneity of the dopant had been ensured, the environment of the dopant was characterized by electron paramagnetic resonance (EPR).

EPR experiments were performed at room temperature to envisage the location of Mn at different possible sites, in the nanocrystal's core or on its surface, in substitutional or interstitial site, since all these locations could be present in the nanocrystals and the EPR hyperfine splitting acts as a sensitive probe for the local environment of manganese [17]. At 300 K, six-line EPR spectra arise due to the hyperfine interaction from the ^{55}Mn nucleus ($I = 5/2$) and correspond to the allowed transition ($\Delta m_s = \pm 1$, $\Delta m_I = 0$), where m_s and m_I are the electron spin and nuclear spin quantum numbers, respectively [4]. The EPR spectra are shown in figure 4 for the different amounts of dopant. For low doping (T1), the spectrum exhibits the expected sextuplet while for higher doping (T2 and T3), the interactions between the spins lead to a broad resonance which overlaps the sextuplet (figure 4(a)). For the sample T1 (0.2% Mn), we have determined the hyperfine splitting constants to be $a = 62$ G, $A = 59 \times 10^{-4}$ cm^{-1} with a gyromagnetic ratio $g = 2.004 \pm 0.001$ at 298 K

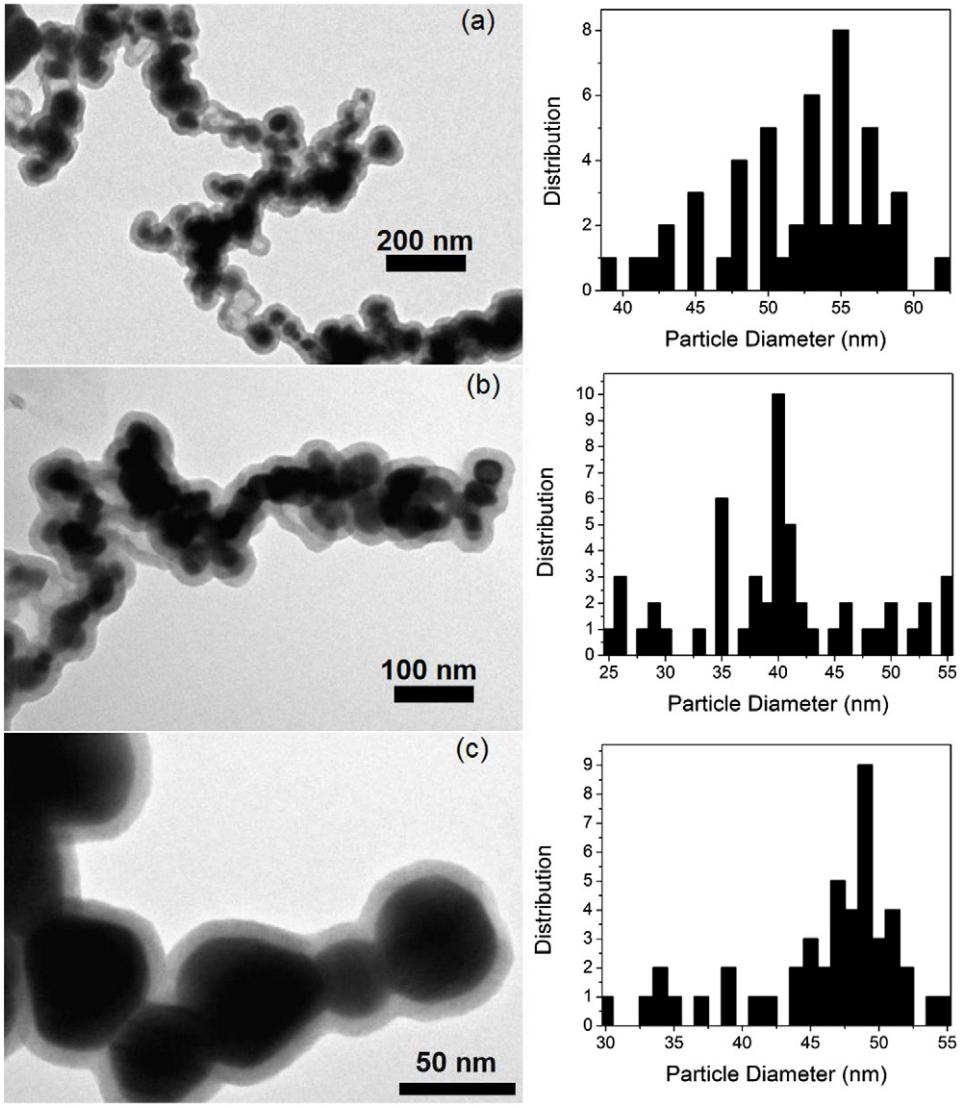

Figure 2. Bright field TEM images of (a) T1, (b) T2, and (c) T3, with the corresponding histograms of nanocrystal size distribution. The higher resolution of the T3 nanocrystals clearly demonstrates the core–shell morphology.

(figure 4(b)). On the other hand, the less diluted samples T2 and T3 (2.4 and 3.1% respectively) display a broad resonance ($\Delta H = 150$ G) also centered at $g = 2.004 \pm 0.001$ at 298 K. For all the samples, the gyromagnetic value found is typical of Mn^{2+} species ($g_0 = 2.000$). The EPR studies allow us to conclude that for all samples the dopant is present in the +II oxidation state. The very low hyperfine splitting value is also consistent with a Mn^{2+} in a tetrahedral environment in the zinc blende lattice of CdTe. Mn^{2+} species on the surface would exhibit a larger splitting ($A = 89 \times 10^{-4}$ cm^{-1}). On the other hand, clusters of MnTe would result in a large ferromagnetic resonance (MnTe is antiferromagnetic with a Néel temperature of 173 K).

A similar environment of Mn^{2+} could be assumed in samples T2 and T3, according to the width of the resonance band, even though EPR cannot rule out the presence of MnTe clusters in these samples. We therefore assume that Mn^{2+} is efficiently doped within the CdTe host lattice and the resonance broadening due to magnetic dipolar interactions. The efficient Mn^{2+} doping and the absence of a 'self-purification' mechanism of manganese could be largely attributed to the larger size of the nanocrystals as compared to the conventional <10 nm DMS nanocrystals [21]. The magnitude of the Mn^{2+} hyperfine splitting constants match with the bulk-like core rather than with ionic surface sites where larger hyperfine splitting persists due to the loss of covalency of the sites occupied by Mn^{2+} [17]. All the doped samples display a narrow band associated with the free radicals on the surface of the carbon coating, the resonance is clearly seen in figure 4(b) (derivative) and could also be observed for the other samples on the derivative curve (not shown). The value of the g-factor ($g = 2.000 \pm 0.001$) and the very narrow line width of $\Delta H = 8$ G are in agreement with the previously reported literature values [20].

The magnetic properties were studied as a function of manganese concentration on the representative samples T1, T2, and T3. Due to close contact between the individual nanocrystals, the magnetic properties are likely to be

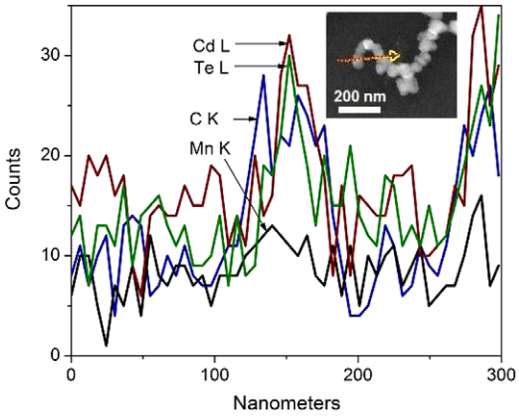

Figure 3. Elemental line scan of the nanocrystals in T3, as shown by an arrow in the SEM image (inset).
(This figure is in colour only in the electronic version)

influenced by the strong interparticle interactions. Figure 5(a) presents the plots of magnetization (M) as a function of applied field $\mu_0 H(T)$ at 300 K. From the nature of the magnetization curves and near saturation at higher fields, it is evident that all the $Cd_{1-x}Mn_xTe$/C samples exhibit ferromagnetism at room temperature. At 300 K, the coercive field values are $\mu_0 H = 6.0$, 5.4, and 2.0 mT for T1, T2, and T3, respectively. At room temperature, the magnetic moment almost reaches saturation for all the samples, which is a signature of predominant ferromagnetic interactions in these systems. However, superparamagnetic fractions due to a distribution of nanocrystal size and/or antiferromagnetic coupling between the manganese atoms in the CdTe matrix are likely to coexist with the ferromagnetic coupling. High field $M(H)$ measurements were also performed at low temperature ($T = 2$ K) and the results are plotted in figure 5(b). All the samples do not display any saturation of the magnetic moment even at an applied field of 6 T. The coercive field values are $\mu_0 H = 49$, 52, and 20 mT for T1, T2, and T3, respectively. The magnetic moments follow a Langevin function $M(H,T) = M_T L(\mu H/K_B T)$ and the hysteresis loops are plotted in Bohr magnetons per manganese atom, the magnetic moment reaches the following values: T1 (1.91 ± 0.02 μ_B/Mn), T2 (0.665 ± 0.008 μ_B/Mn), and T3 (0.383 ± 0.005 μ_B/Mn). The expected magnetic moment of a free Mn atom in the +II valence state is 5.92 μ_B, adding the spin and orbital contributions. Nevertheless, the Langevin fit of $M(H)$ curves at 2 K gives lower values. The magnetic moment of manganese molecular species indeed reflects the spin moment 5/2. However, that is not the case for manganese ions in interactions, for instance, in the case of diluted manganese systems with a concentration x. The magnetic field H can be described by a modified Brillouin function with two empirical parameters $x_{\text{eff}} < x$ and $T_{\text{eff}} = T + T_{\text{AntiFerromagnetic}}$ that take into account the antiferromagnetic super-exchange interaction between the Mn spins [22, 23].

The observation of the highest magnetic moment in the lowest Mn doped sample, T1 (1.91 ± 0.02 μ_B/Mn) compared to T2 (0.665 ± 0.008 μ_B/Mn), and T3 (0.383 ± 0.005 μ_B/Mn) is the best evidence that Mn is distributed in the interior of the CdTe lattice and not present as Mn clusters at the surface of the nanocrystals. The ferromagnetism in all the samples arises from the manganese spins distributed in the CdTe semiconductor and not from manganese clusters. The more concentrated samples (T2 and T3), which are more likely to present Mn clusters according to EPR measurements, exhibit weaker ferromagnetic interactions probably due to an incomplete coupling between carriers and spins. A similar observation was earlier found in Mn doped TiO_2 nanocrystals, where the higher doped samples become paramagnetic [20]. Moreover, the magnetic coupling between two Mn atoms in a bulk semiconductor is a function of the Mn–Mn distance and relative positions of the Mn^{2+} ions, and oscillates between positive (ferromagnetic) and negative (antiferromagnetic) values with the increase in doping concentration [24]. Based on this theoretical model, the coupling constant in CdTe: Mn^{2+}/C nanocrystals remains nearly positive at all distances beyond Mn–Mn nearest neighbors. At lower doping levels of Mn^{2+} studied in this paper, isolated Mn^{2+} ions exist in the partially substituted $Cd_{1-x}Mn_xTe$ lattice, whereby ferromagnetic coupling between the isolated Mn^{2+} spins is dominant.

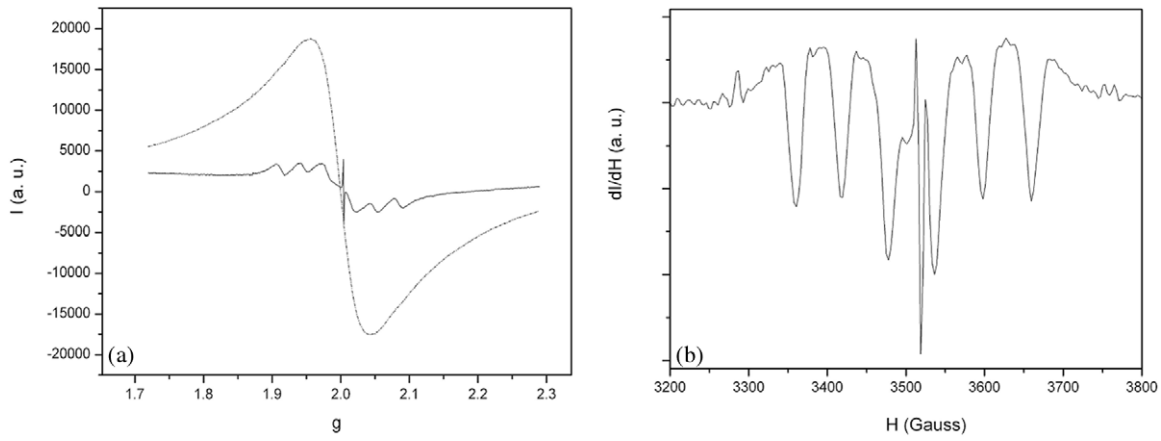

Figure 4. EPR spectra of $Cd_{1-x}Mn_xTe$/C samples at 300 K. Samples T1 (solid line) and T2 (dashed line) (a) and the first derivative of the EPR spectrum for sample T1.

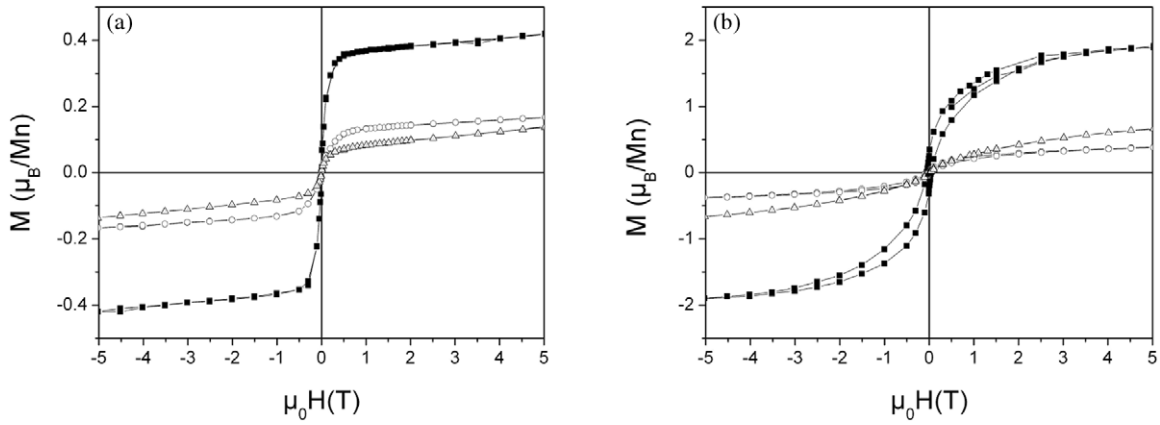

Figure 5. Magnetization curves at (a) $T = 300$ K, and (b) $T = 2$ K for the samples T1 (plain squares), T2 (hollow dots), and T3 (hollow triangles).

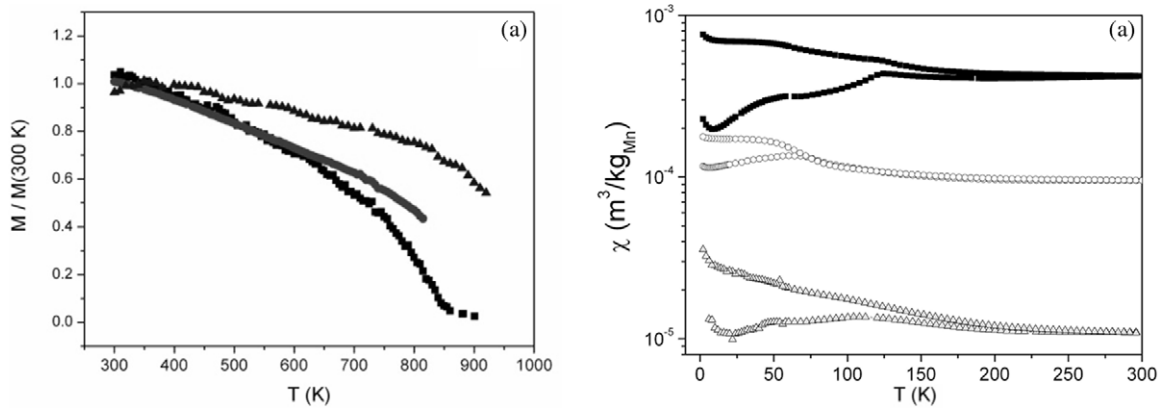

Figure 6. (a) Susceptibility at high temperature (VSM, 300–1000 K, $\mu_0 H = 2$ T) and (b) susceptibilities ZFC/FC at low temperature (2–300 K), for samples T1 (squares), T2 (dots), and T3 (triangles).

To get further insight into the magnetic properties of the samples, we have performed high temperature susceptibility measurements (300 to around 900 K) using a vibrating sample magnetometer. Surprisingly, the observed ferromagnetism is very robust with a very high Curie temperature (figure 6(a)). The magnetic moments have been plotted as M/M (300 K) for an easier comparison of the behavior of the three systems. The magnetic moment measured at 300 K is comparable to the one measured with the SQUID with values in the range of 10^{-3}–10^{-2} emu (with about 10–50 mg of powder). For the most diluted sample, the Curie temperature is found to be close to 850 K, it has to be noticed that this temperature does not correspond to any of the impurities like MnTe (antiferromagnetic, $T_N = 173$ K) and Fe (ferromagnetic, $T_C = 1043$ K). The Curie temperature could match that of magnetite but the other samples clearly show a higher Curie temperature. Furthermore, this would mean that all the magnetic contributions observed arise from this magnetic impurity (which would correspond to 0.2% of magnetite in the sample and would be detected by ICP analysis). The Curie temperature of samples T2 and T3 were above the highest stable temperature reached during the experiment. Nevertheless, the trend in magnetic properties of the samples clearly shows that the robustness of ferromagnetism increases with the dopant concentration.

The magnetic susceptibility was investigated using a ZFC/FC routine at a field of $\mu_0 H = 0.02$ T. Figure 6(b) shows the susceptibility plotted as a function of temperature (log scale for the Y axis). The magnetic susceptibility does not follow a Curie–Weiss law, which clearly eliminates the possibility of a paramagnetic behavior. At low temperature, a slight increase of the susceptibility could be ascribed to uncoupled Mn spins. Over all the temperature range, the ZFC and FC plots do not overlap which is additional evidence for exchange interactions. The ZFC plots for all the samples show humps below 120 K (56 and 120 K for T1; 60 K for T2; 47 and 111 K for T3) which could be due to antiferromagnetic regions, displaying a locally higher content of Mn. This behavior is consistent with the lower magnetic moment found for the Mn as compared to the free Mn^{2+} ion. The exact nature of this magnetic ordering is not ascertained in this study; however, localized short-range magnetic ordering and magnetic dipolar interactions are highly probable at lower temperatures [25, 26]. Even if these low temperature anomalies could also have been ascribed to a local discrepancy between the doping concentrations of Mn^{2+} ions in the CdTe matrix, the remarkable temperatures do not correspond to any phase transition temperature of the potential

secondary phase mentioned above (Fe and MnTe). The role of carbon, as pointed out in our previous studies, does not seem to be predominant in the magnetic properties of the samples.

4. Conclusions

In conclusion, carbon-encapsulated $Cd_{1-x}Mn_xTe$ nanocrystals with Mn at.% of 0.2, 2.4, and 3.1 were synthesized by the one-step solid state reaction inside a closed reactor at 1000 °C. The mechanism for the formation of the core–shell nanocrystals, without the use of any template, is a kinetically controlled process involving the $Cd_{1-x}Mn_xTe$ nucleus formation and 6–9 nm thick carbon encapsulation. The 40–52 nm core of the $Cd_{1-x}Mn_xTe$/C products has a zinc blende crystal structure and Mn^{2+} is efficiently and uniformly doped inside the CdTe nanocrystals until a Mn:Cd atomic ratio of 0.031, as evidenced from the room temperature EPR measurements. Ferromagnetism was observed for all the doped samples, the magnetic moment being the highest in the 0.2% doped sample (1.91 ± 0.02 μ_B/Mn) compared with that of 2.4% (0.665 ± 0.008 μ_B/Mn), and 3.1% (0.383 ± 0.005 μ_B/Mn). This might be due to an incomplete coupling between carriers and spins. The ferromagnetic interactions are stable until high temperatures and the paramagnetic transition occurs above 800 K.

Acknowledgments

The authors thank the platform of the Institute Charles Gerhardt of Montpellier (France) and C Reibel for conducting the EPR, SQUID, and VSM experiments.

References

[1] Zutic I, Fabian J and DasSarma S 2004 *Rev. Mod. Phys.* **76** 323–410
[2] Dietl T, Haury A and d'Aubign'e Y M 1997 *Phys. Rev.* B **55** R3347–50
[3] Dietl T, Ohno H and Matsukura F 2001 *Phys. Rev.* B **63** 195205
[4] Erwin S C, Zu L, Haftel M I, Efros A L, Kennedy T A and Norris D J 2005 *Nature* **436** 91–4
[5] Yang H, Santra S and Holloway P H 2005 *J. Nanosci. Nanotechnol.* **5** 1364–75
[6] Shan J and Xue-chu S 1994 *Acta Phys. Sin.* **3** 925–31
[7] Besombes I, Léger Y, Maingault L, Ferrand D, Bougerol C, Mariette H and Cibert J 2005 *Acta Phys. Pol.* A **108** 527–40
[8] Banerjee P and Ghosh B 2008 *J. Phys. Chem. Solids* **69** 2670–3
[9] Kwak W C, Sung Y M, Kim T G and Chae W S 2007 *Appl. Phys. Lett.* **90** 17311
[10] Rogach A L, Franzl T, Klar T A, Feldmann J, Gaponik N, Lesnyak V, Shavel A, Eychmüller A, Rakovich Y P and Donegan J F 2007 *J. Phys. Chem.* C **111** 14628–37
[11] Tsuruoka T, Takahashi R, Nakamura T, Fijii M, Akamatsu K and Nawafune H 2008 *Chem. Commun.* 1641–3
[12] Kuo Y–C, Wang Q, Ruengruglikit C, Yu H and Huang Q 2008 *Phys. Chem.* C **112** 4818–24
[13] Sgobba V, Schulz-Drost C and Guldi D M 2007 *Chem. Commun.* 565–7
[14] Geng B Y, Du Q B, Liu X W, Ma J Z, Wei X W and Zhang L D 2006 *Appl. Phys. Lett.* **89** 033115
[15] Bhattacharyya S, Perelshtein I, Moshe O, Rich D H and Gedanken A 2008 *Adv. Funct. Mater.* **18** 1641–53
[16] Bhattacharyya S, Estrin Y, Moshe O, Rich D H, Solovyov L A and Gedanken A 2009 *ACS Nano* **3** 1864–76
[17] Bhattacharyya S, Zitoun D and Gedanken A 2008 *J. Phys. Chem.* C **112** 7624–30
[18] Bhattacharyya S and Gedanken A 2008 *J. Phys. Chem.* C **112** 4517–23
[19] Bhattacharyya S, Zitoun D, Estrin Y, Moshe O, Rich D H and Gedanken A 2009 *Chem. Mater.* **21** 326–35
[20] Bhattacharyya S, Pucci A, Zitoun D and Gedanken A 2008 *Nanotechnology* **19** 495711
[21] Zu L, Norris D J, Kennedy T A, Erwin S C and Efros A L 2006 *Nano Lett.* **6** 334–40
[22] Clavel G, Willinger M G, Zitoun D and Pinna N 2008 *Eur. J. Inorg. Chem.* **6** 863–8
[23] Furdyna J K 1988 *J. Appl. Phys.* **64** R29
[24] Chen H, Zhu W, Kaxiras E and Zhang Z 2009 *Phys. Rev.* B **79** 235202
[25] Gajbhiye N S and Bhattacharyya S 2007 *J. Appl. Phys.* **101** 113902
[26] Gajbhiye N S and Bhattacharyya S 2007 *Japan. J. Appl. Phys.* **46** 980–7